ADVANCED FUNCTIONAL MATERIALS
www.afm-journal.de

A Micro Battery Supercapacitor Hybrid Device with Ultrahigh Cycle Lifespan and Power Density Enabled by Bi-Functional Coating Design

Fazhi Ye, Wei Yang, Xiaobin Liao, Chenhui Dong, Lin Xu,* and Liqiang Mai**

Micro energy storage devices (MESDs) have emerged as promising energy providers for micro applications due to their integrated performance. However, the limited cycle life and low power density of microbattery, and low energy density of microsupercapacitor have consistently impeded their broader practical implementation. Herein, to obtain a MESD with a long cycle life, excellent power density, and superior energy density, a novel micro battery-supercapacitor hybrid (MBSH) device is fabricated. Two types of 3D microelectrodes are fabricated, namely, a nanowire network anode based on PEDOT-TiON and a porous cathode based on $Ni(OH)_2$. Benefiting from the unique hydrophobic characteristics of the PEDOT layer, high electrical conductivity of TiON, and high conductivity, and abundant ion diffusion channels of network microstructure, PEDOT-TiON NW microelectrodes demonstrate exceptional cycling stability by retaining 70% of their capacity after 40 000 cycles. The achieved MBSH exhibits an extended voltage window ranging from 0 to 1.9 V, impressive power density of 77.5 mW cm^{-2}, and a superior energy density of 55.6 µWh cm^{-2}. Furthermore, it maintains a remarkable capacity retention rate of 71.6% even after undergoing 30 000 cycles. This innovative design paves the way for the developing of high-performance microdevices with superior electrochemical properties.

1. Introduction

The advancement of intelligent electronic applications, such as implantable medical sensors, wireless self-powered systems, and the Internet of Things (IoT), has created an urgent need for microenergy storage devices (MESD).[1] In recent decades, microbatteries (MBs) and microsupercapacitors (MSCs) have emerged as the two most promising types of MESDs for next-generation microelectronic device applications. MBs, such as micro lithium-ion batteries, typically exhibit a high energy density of ≈1 mWh cm^{-2}. Due to the slow and diffusion-controlled electrochemical process, MBs exhibit low power density (<5 mW cm^{-2}) and poor cycling performance (500–2000 cycles).[2] Among them, zinc-ion MBs are expected to be the next-generation eco-friendly aqueous MESDs. However, due to the uncontrolled growth of zinc dendrites, the cycle performance of MBs has been severely hindered.[3] Alternatively, despite the advantages of high power density (>10 mW cm^{-2}) and optimum cycling performance (even $>10^6$ cycles), a lack of energy density has limited the broader application situation of MSCs to a great extent.[4] To this end, there is an urgent need to develop a micro battery-supercapacitor hybrid device (MBSH) that can combine the advantages of both a battery-type electrode and a capacitor-type electrode.[5] Meanwhile, researchers have made significant efforts to select matched cathode and anode materials in order to achieve higher energy density, power density, and extended cycle life for MBSH, thereby meeting the requirements of various applications.

In general, by increasing the voltage window and capacity of MBSH, the energy density can be maximized according to the formula $E = 1/2CV^2$.[6] Among active materials for MBSH electrodes, transition metal nitride materials have garnered significant attention due to their ability to offer a wide voltage window. Furthermore, these materials contain nitrogen atoms that facilitate the dense packing of metal atoms within the lattice structure, thereby promoting high electronic conductivity.[7] Among them, Titanium nitride oxide (TiON) material exhibits an impressive electronic conductivity of up to 55 500 S cm^{-1}, highlighting its strong affinity for nitrogen atoms and bonding capability.[8] However, this characteristic also contributes to a certain level of chemical inertness in the pristine TiON material, leading to relatively low capacity (<10 mF cm^{-2}).[9] Furthermore, previous studies have revealed the inadequate performance of TiON material during the charging/discharging cyclic process conducted in aqueous alkaline electrolytes (<5000 cycles),[10] due to the irreversible side reaction of TiON with TiO_2 ($TiN + 2H_2O \rightarrow TiO_2 + 1/2N_2 + 4H^+ + 4e^-$). In recent years, remarkable efforts have been made to address these issues of low capacity and poor cycling

F. Ye, W. Yang, X. Liao, C. Dong, L. Xu, L. Mai
State Key Laboratory of Advanced Technology for Materials Synthesis and Processing
School of Materials Science and Engineering
Wuhan University of Technology
Wuhan 430070, China
E-mail: yangwei830@whut.edu.cn; linxu@whut.edu.cn; mlq518@whut.edu.cn

The ORCID identification number(s) for the author(s) of this article can be found under https://doi.org/10.1002/adfm.202413379

DOI: 10.1002/adfm.202413379

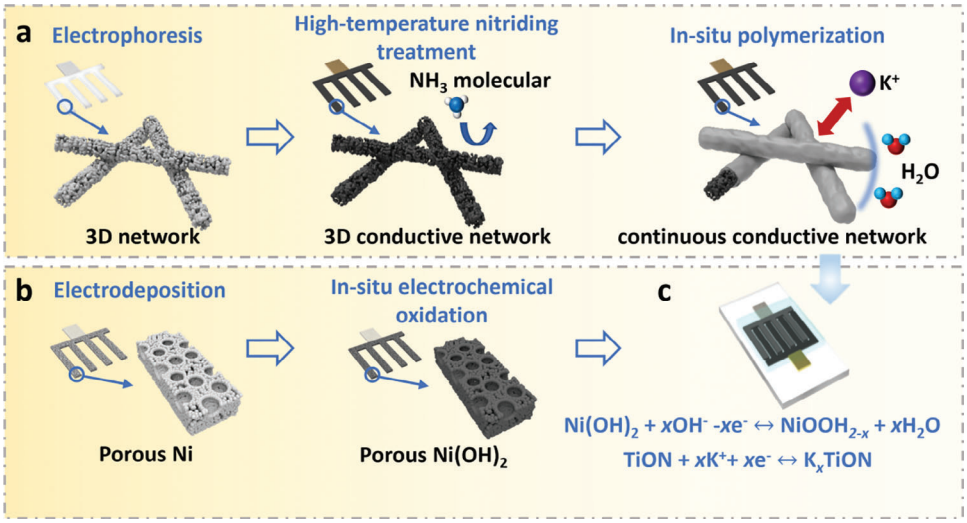

Figure 1. The Fabrication schematic diagram. a) A three-step synthesis of PEDOT-TiON microelectrode using electrophoresis, high-temperature nitriding treatment, and in situ polymerization. b) A two-step in situ electrochemical oxidation of $Ni(OH)_2$ porous microelectrode. c) Assembled MBSH device.

performance. For instance, Qi et al. employed a nanohybrid approach to prepare TiN/VG, resulting in enhanced cycling performance (89.5% capacity retention after 10 000 cycles.) and achieving a specific capacitance of 9.0 mF cm^{-2} at 100 mV s^{-1}.[11] In contrast, Fang et al. utilized a composite strategy with high pseudocapacitive materials to obtain MnO_2-TiN, which significantly improved capacitive performance (213.2 mF cm^{-2} at 0.25 mA cm^{-2}) with a retention rate of 92.7% after 200 cycles under aqueous alkaline electrolyte.[12] However, all these strategies have proven inadequate in simultaneously enhancing the capacitance performance and improving the cycling stability of TiON materials. Therefore, it is imperative to investigate the capacity decay mechanism of TiON materials in aqueous alkaline electrolytes while developing effective approaches to optimize electrode materials. These approaches should ensure both excellent electronic conductivity of TiON itself and enhanced surface ion transport, thereby achieving a high pseudocapacitive capacity while maintaining structural integrity during long-term cycles. To cope with these issues, introducing a hydrophobicity polymer coating layer is a promising and facile way. Among the various reported polymers, the PEDOT can meet the following requirements, i) low polymerization temperature for the simple synthesis procedure; ii) excellent conductivity to guarantee efficient ion transport and charge transfer; iii) robust mechanical properties and compatibility with the active materials to form a hydrophobic integrated structure.[13]

Herein, we constructed a MBSH with a KOH alkaline electrolyte, in which the PEDOT-TiON nanowire network anode provides abundant pathways for electrolyte diffusion and serves as an interface for electrochemical reaction with potassium ion. The PEDOT layer facilitates rapid electron conduction through an additional pathway, while its unique bi-functional structure effectively prevents water molecule infiltration without impeding potassium ion insertion. This decelerates the oxidation of the anode during charge–discharge processes, ensuring a long cycling life for PEDOT-TiON NW microelectrode in alkaline electrolytes. As a result, the resulting PEDOT-TiON//$Ni(OH)_2$ MBSH device exhibits extraordinary cycle stability with 71.8% capacity retention after 30 000 cycles. Consequently, the PEDOT-TiON//$Ni(OH)_2$ based MBSH device displays a wide voltage window (0–1.9 V), high energy density, and high power density (55.6 μWh cm^{-2} at 77.5 mW cm^{-2}).

2. Results and Discussion

The fabrication processes of the PEDOT-TiON//$Ni(OH)_2$-based MBSH are schematically illustrated in **Figure 1**. First, a 3D $H_2Ti_3O_7$ nanowire network was fabricated through an electrophoresis process on a mass-customized Ti interdigital microelectrode. After undergoing high-temperature nitriding treatment, a high-mass-loading 3D nanowire network was achieved with high mass-loading of TiON nanowires is achieved. The TiON nanowire network aggregates serve as pathways for electron conduction, providing a large surface area for conductive polymer growth and continuous internal channels for electrolyte diffusion. To fabricate a continuous electron conductive path, a dense cross-linked polymer film of PEDOT is constructed on the surface of the TiON nanowires through an in situ growth process (Figure 1a; Figure S1, Supporting Information), as described in our previous work.[14] Then, the $Ni(OH)_2$ nanostructure microelectrode was prepared on the surface of a Ni interdigital microelectrode using a two-step electrochemical preparation approach (Figure 1b). Eventually, the PEDOT-TiON//$Ni(OH)_2$ MBSH device was obtained after covering an alkaline KOH gel-electrolyte on the interdigital microelectrodes (Figure 1c).

The morphology and microstructure of the pure TiON nanowire microelectrode were examined using scanning electron microscopy (SEM), as shown in **Figure 2a**. The Ti interdigital microelectrode is uniformly covered by TiON nanowires with a homogeneous microstructure. Figure 2b exhibits the continuous and compact structure as well as homogeneous pores of TiON nanowires coated with PEDOT. The transmission electron microscope (TEM) and high-angle annular dark fields (HAADF) images in Figure 2b,c demonstrate that the conductive

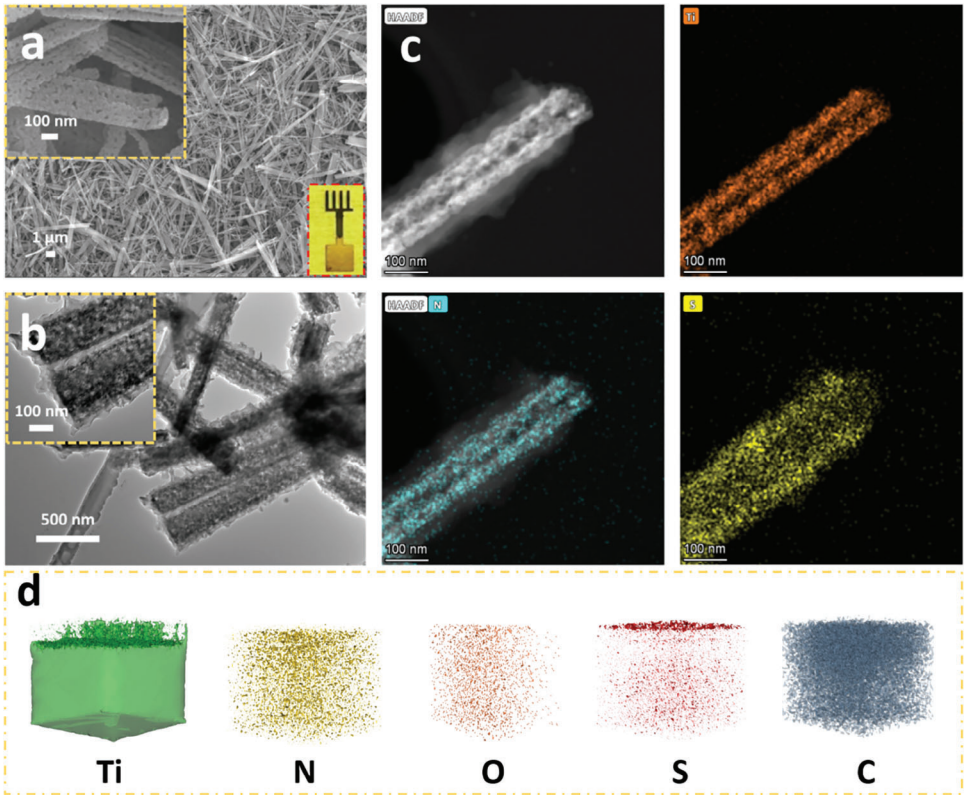

Figure 2. The morphology and microstructure of PEDOT-TiON and $Ni(OH)_2$ microelectrode. a) SEM image of pristine TiON NW microelectrode and optical images (insert). b,c) TEM and HAADF images of PEDOT-TiON NW microelectrode. d) TOF-SIMS images of PEDOT-TiON.

polymer of PEDOT is firmly anchored on the TiON nanowires, with a polymer layer thickness of ≈30 nm. In TEM images, the high-intensity region corresponds to the core of a single nanowire, while the surrounding low-intensity area represents the coating layer. In the HAADF images of Ti elements, a uniform distribution is observed within the core region of the nanowires. The N element exhibits a distribution pattern similar to Ti, predominantly occupying the core region. Correspondingly, the S element exhibits a significantly broader distribution range that encompasses both the core and edge regions of the nanowires, aligning within the area occupied by PEDOT. These findings demonstrate consistent and homogeneous material transformation during nitriding, as well as uniform growth during PEDOT coating. Furthermore, the pristine TiON nanowires exhibit typical single-crystal characteristics (see Figure S3, Supporting Information), while the SAED pattern of PEDOT-TiON nanowires still shows distinct diffraction spots on the TiON lattice planes.[15] To better confirm the chemical component of the anode on the surface and inner structure, we analyzed the PEDOT-TiON using the time-of-flight secondary-ion mass spectrometry (TOF-SIMS). In Figure S4 (Supporting Information), the secondary fragments of Ti, N, S, and O elements were detected and depicted in TOF-SIMS ion images after undergoing the ion beam etching. In Figure 2d, the TOF-SIMS 3D rendering models showed the even distribution of Ti, N, S, O, and C elements in the PEDOT-TiON microstructure, which strongly accords with the above conclusions. The X-ray diffraction patterns are also consistent with the expected results, which belong to TiN (PDF# 87–0632) and TiO (PDF# 77–2170), seeing Supporting Information Figure S2 (Supporting Information). These results provide evidence of the successful preparation of the PEDOT-TiON NW microelectrode, and it was observed that the in situ polymerization process does not induce oxidation of TiON. As for $Ni(OH)_2$ microelectrodes, the SEM images have presented the ordered 3D porous microstructure with a diameter of ≈10 μm, and the nanostructure can be evenly distributed on the surface of large porous, which provides an abundant surface for the chemical reaction (Figure S5, Supporting Information). Moreover, combined with the XPS spectrum, the presence of Ni, C, and O elements can be observed. While the C peak is from the reference carbon, Ni and O elements are located on the surface of $Ni(OH)_2$ microelectrode. Figure S6 (Supporting Information) exhibits a detailed XPS peak position of Ni 2p that accurately conforms to the former study, showing Ni 2p1/2 and Ni 2p3/2 levels arose at two prominent Binding energy peaks of 873.5 and 855.9 eV. Moreover, the spin-energy separation of 17.6 eV corresponds to the feature of $Ni(OH)_2$, verifying the existence of $Ni(OH)_2$ in the microelectrode.[16] Meanwhile, in the XPS spectrum of O 1s, the central XPS peak is 531.5 eV which belongs to the OH^- groups originating from Ni $(OH)_2$, and the other weaker peak in 532.9 eV provides an additional oxygen contribution.[17] These results perfectly demonstrate that the $Ni(OH)_2$ nanostructure microelectrode has been successfully fabricated.

The electrochemical performances of PEDOT-TiON and $Ni(OH)_2$ microelectrodes were investigated using a three-electrode system with a concentration of 1 M KOH in an

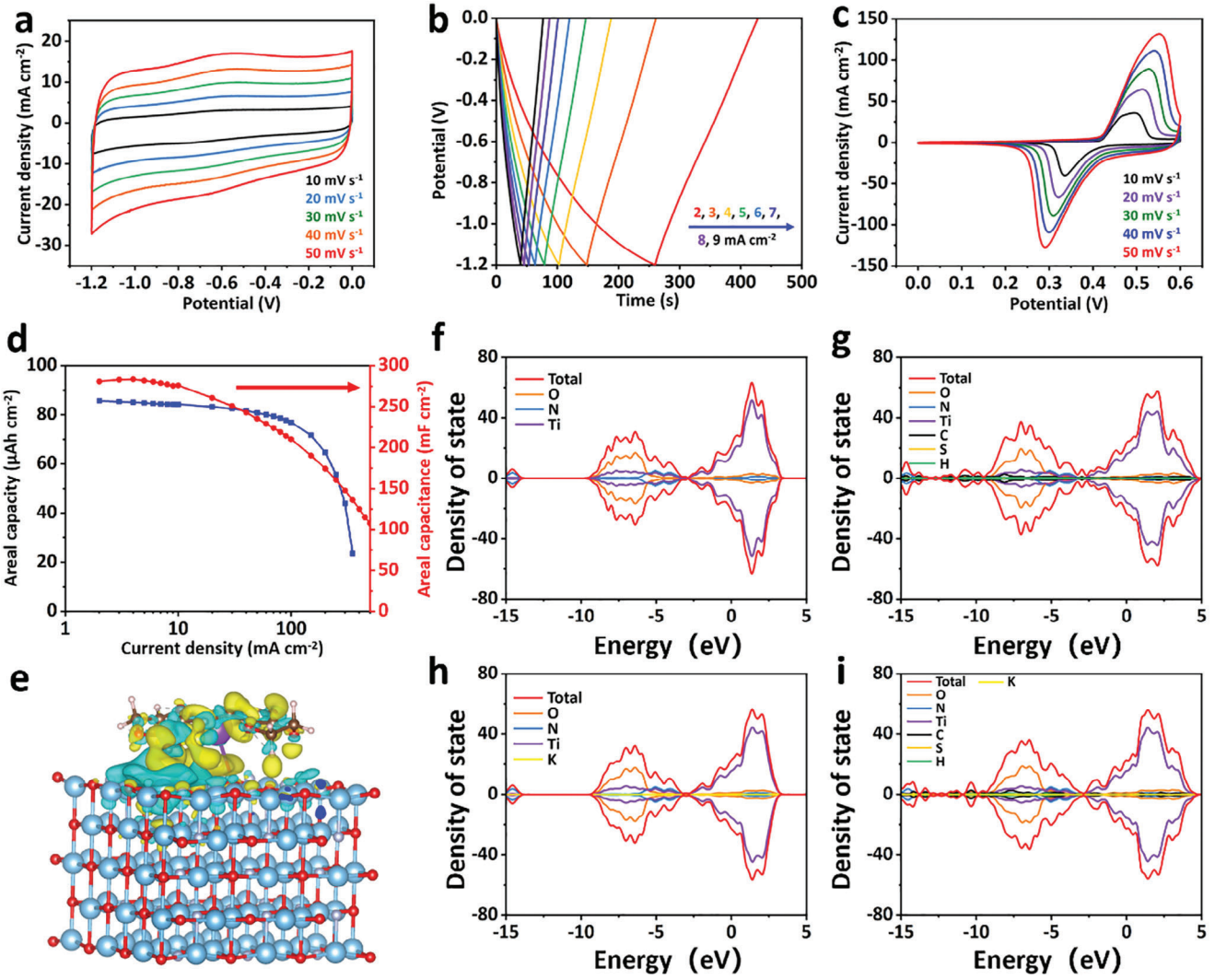

Figure 3. a,b) CV and GCD curves of PEDOT-TiON nanowire microelectrode. c) CV curves of $Ni(OH)_2$ nanostructure microelectrode. d) Areal capacity/capacitance of PEDOT-TiON NW and $Ni(OH)_2$ nanostructure microelectrodes at different current densities. e) The charge density difference iso-surface of the PEDOT-TiON interface. DOS of f) TiON, g) PEDOT-TiON, h) TiON adsorbed K^+ ions and i) PEDOT-TiON adsorbed K^+ ions.

aqueous electrolyte. As depicted in **Figure** 3a, the cyclic voltammetry (CV) curves obtained from the PEDOT-TiON nanowire microelectrode demonstrate excellent capacitance behavior when scanned at rates ranging from 10 to 50 mV s^{-1}. The CV curves with symmetrical rectangular shapes indicate a pseudocapacitive mechanism and efficient electron conduction. Compared to the CV curve of the pure TiON nanowire microelectrode (see Figure S8a, Supporting Information), the PEDOT-TiON microelectrode exhibits lower polarization at high voltages, particularly when subjected to a low scan rate of 10 mV s^{-1}. The electrochemical impedance spectroscopy (EIS) curves of the TiON microelectrode and PEDOT-TiON microelectrode in Figure S9b (Supporting Information) exhibit a significant reduction in equivalent series resistance following the introduction of the PEDOT conductive layer nanowires network. The GCD curves of PEDOT-TiON nanowires microelectrode with quasi-triangle shape are shown in Figure 3b and Figure S8 (Supporting Information), demonstrating the boosted capacitance of 280.6 mF cm^{-2} at 2 mA cm^{-2}. When the current density increases gradually from 2 mA cm^{-2} to the ultrahigh 500 mA cm^{-2}, standard triangular GCD curves are displayed, indicating excellent pseudocapacitance characteristics. These high capacitance and outstanding capacitance retention at high current density indicate the high-mass-loading 3D network structure, which reveals excellent electron/ion transfer performance and a large surface area for electrochemical reactions. Meanwhile, the kinetics measurement based on CV curves (from 1 to 5 mV s^{-1}) was carried out to further understand the potassium-ion storage mechanism of PEDOT-TiON (Figure S10, Supporting Information), executed using the following formula:

$$i = k_1 v + k_2 v^{1/2} \quad (1)$$

where $k_1 v$ represents the capacitive effects, $k_2 v^{1/2}$ refers to diffusion-controlled, and the peak current i varies with the variation of $v^{1/2}$ (v is the scan rate, V s^{-1}).[18] The disparity between

the area enclosed by the two CV curves represents capacitive contribution and total capacitance. The shaded area was obtained by calculating the function of capacitive current response ($k_1\nu$) and potential. Furthermore, at a scan rate of 2 mV s^{-1}, the capacitive-controlled process contributes significantly with a percentage of 84.8%, and as the scan rate increases, capacitive contribution becomes even more prominent. The pseudocapacitance reaction dominates the total capacitance when it increases to 90.0% at a scan rate of 5 mV s^{-1}. It is further revealed that introducing the robust PEDOT conductive polymer has vividly boosted higher rate capability. In Figure 3c, the CV curves of $Ni(OH)_2$ microelectrode retain similar sharpness even at a high scan rate of 50 mV s^{-1}. This ultrahigh reaction kinetics indicates the porous structure offering a large surface area for the battery-type reaction mechanism with OH^-. The GCD curves also show the high coulombic efficiency redox plateau within the voltage window of 0–0.6 V, corresponding to the CV results (Figure S11, Supporting Information). Figure 3d shows the areal capacity retention rates of the $Ni(OH)_2$ nanostructure microelectrode and the PEDOT-TiON nanowire microelectrode at different current densities. The PEDOT-TiON microelectrode still has a responsive electrochemical capacity at the ultra-high charge-discharge current density of 100–500 mA cm^{-2}, showing excellent pseudo capacitance and power characteristics.

Density functional theory simulations on the TiON and PEDOT-TiON were conducted to investigate the interactions between different components. Differential charge density is shown in Figure 3e. The image displays electron accumulation (yellow) and depletion (blue) regions, revealing the efficient electronic transfer channel from C, H, and S atoms in the PEDOT to TiON, with electron accumulation concentrated around Ti atoms. This phenomenon aligns with density of states (DOS) results and confirms that in situ PEDOT encapsulation significantly improves TiON NW microelectrodes' electronic conductivity. As shown in Figure 3f, TiON exhibits a continuous DOS at the Fermi level, indicating its conductive properties. After introducing PEDOT onto the surface of TiON, the total DOS is enhanced at the Fermi level (Figure 3g), and the unoccupied states of Ti element rise, suggesting an increase in free electron concentration within the system. This indicates that PEDOT interacts with TiON to enhance electronic conductivity.[19] In comparison to pure TiON surfaces, there is no significant change in DOS results after surface modification with K elements alone (Figure 3h), indicating that introducing a single K 1s impurity orbital does not significantly improve the electronic conductivity of TiON nanowire. Figure 3i shows the DOS curve after modifying the TiON surface with both K and PEDOT. Due to the introduction of K atoms between the PEDOT and TiON interface, the charge transfer pathway increases, and unoccupied energy levels slightly rise compared to the PEDOT-TiON system, leading to further enhancement in ions conductivity and low polarization. Based on these results, we can conclude that by introducing the PEDOT layer, PEDOT-TiON microelectrodes exhibit better cycle life and higher scan capability than pristine TiON NW microelectrodes.

As mentioned previously, during the discharge/charge process, the highly active free water molecular will insert the structure of TiON materials and then irreversible oxidation occurs. Here, in **Figures** 4a and S12 (Supporting Information), the pristine TiON nanowire electrode undergoes rapid polarization when cycled in 1 M KOH electrolyte at a current density of 10 mA cm^{-2}, resulting in a limited voltage window that fails to reach −1.2 V after only 2000 cycles. In contrast, it is evident that the PEDOT-TiON nanowire electrode, designed using an in situ hybrid strategy, exhibits remarkable durability, withstanding up to 40 000 cycles under identical conditions while maintaining a capacity retention rate of 70%. This preliminary experiment validates the feasibility and practicality of the in situ hybrid design strategy. To explore the underlying role of the PEDOT layer, ex situ Raman spectrum characterizations on PEDOT-TiON nanowires microelectrode after long-term cycles were conducted in Figure 4b,c. All Raman peaks were assigned based on those from the referenced TiON and PEDOT. The prominent Raman peaks, ranging from 100 to 600 cm^{-1}, are attributed to typical Anatase TiO_2 vibrations (143, 515 cm^{-1}) and Ti-N vibrations (206, 441, 570 cm^{-1}), respectively.[20] One strong peak at 143 cm^{-1} is caused by O-Ti-O bending vibration mode, while the Raman peak at 515 cm^{-1} corresponds to O-Ti-O anti-symmetric bending as the main vibration supplemented by symmetric stretching vibration.[21] Meanwhile, the new peak at 1527 cm^{-1} originated from the C═C asymmetrical stretching, while the peak at 1440 cm^{-1} is associated with the symmetrical stretching of C═C. The peaks of C—C stretching, C—C inter-ring stretching mode, C—O—C bond deformation, and C—C antisymmetric stretching are at 1365, 1269, 1099 and 988 cm^{-1}, respectively.[22] Consequently, these results confirm that conductive polymer PEDOT has been successfully coated onto TiON nanowire. An obvious Raman peak conversion was observed after a long-term charge/discharge process. TiON nanowires exhibited enhanced Ti-O and degraded Ti-N Raman signals. In contrast, the cycled PEDOT-TiON nanowires maintained their structure stability without any noticeable difference in Raman shift. The N1s and O1s XPS spectrum of TiON and PEDOT-TiON, before and after cycling, further validate the crucial role played by the PEDOT coating layer (Figure S15, Supporting Information). The N 1s XPS peak of the TiON material was observed to diminish following an extended cycling period. Conversely, cycled PEDOT-TiON still exhibits prominent N-Ti-O and N-Ti peaks, providing compelling evidence for its exceptional cycle stability. Following long-term cycling, the O 1s XPS spectrum of cycled-TiON microelectrode reveals two distinct peaks at 529.8 and 531.6 eV corresponding to crystalline oxygen (Ti—O bond) and hydroxyl oxygen (Ti—OH), respectively. These findings suggest an irreversible side reaction between TiON and KOH aqueous electrolyte; however, cycled-PEDOT-TiON demonstrates enhanced structural integrity and compositional stability due to its bi-functional PEDOT coating layer. Furthermore, Density Functional Theory (DFT) was employed for calculating the adsorption energies of free water molecules (H_2O) and potassium ions (K^+) at various sites on PEDOT-TiON and TiON (see supporting information Figure S13, Supporting Information). Simultaneously, Figure 4d illustrates the corresponding absorption sites of two models, demonstrating that stable absorption energies occur between free water molecules and the PEDOT-TiON composite as well as at the interface of TiON nanowires. This observation confirms that free water molecules are more readily inserted into the TiON nanowires, while the PEDOT-TiON composite exhibits weaker adsorption behavior toward free water molecules. As shown in Figure S14 (Supporting Information), the contact angle of the electrolyte (1 M KOH) on the PEDOT-TiON anode

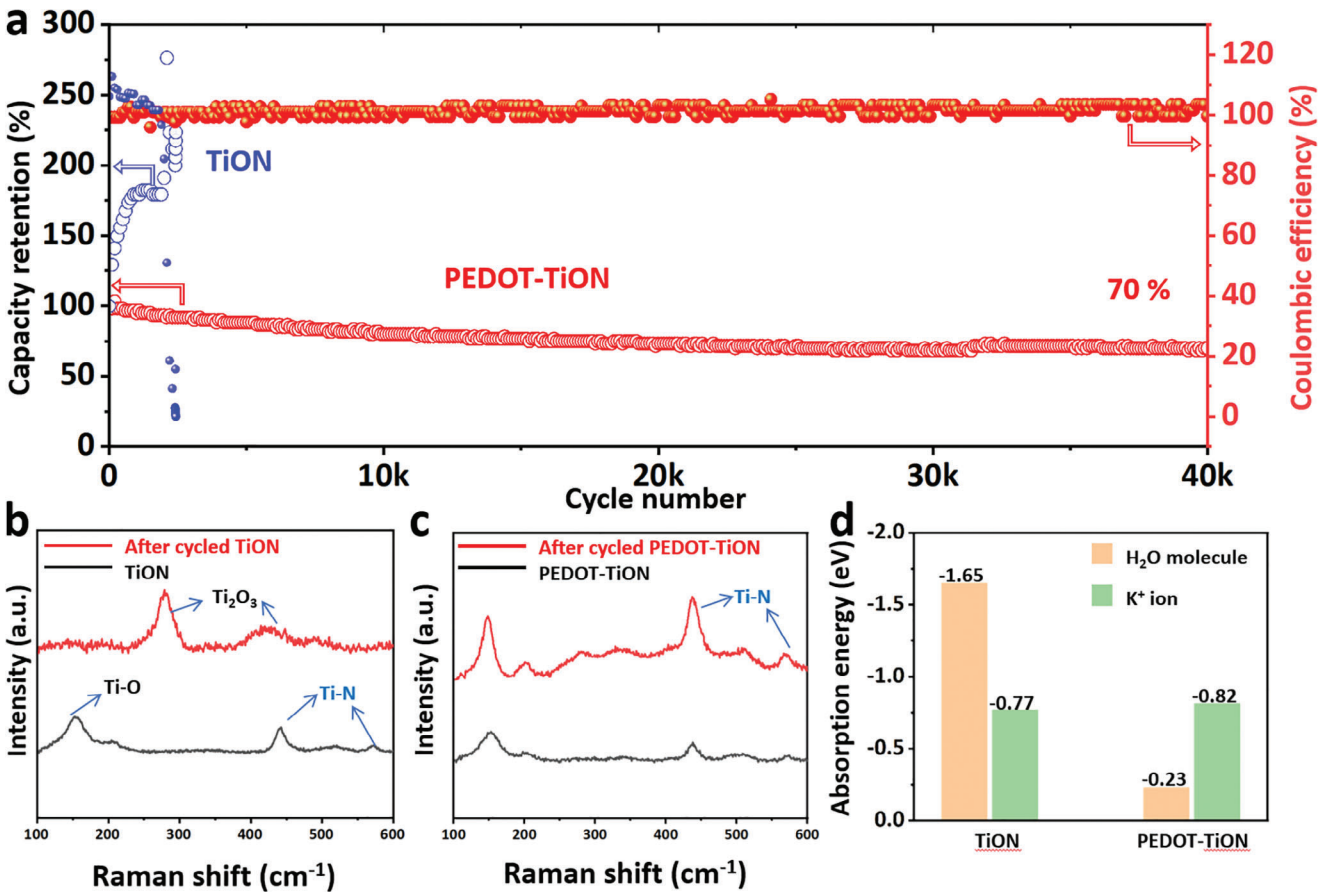

Figure 4. a) Cycling performances of TiON and PEDOT-TiON microelectrodes. Raman spectrum of pristine and cycled microelectrodes b) TiON NW microelectrode, c) PEDOT-TiON NW microelectrode. d) Adsorption energy of H_2O molecule and K^+ ion on the TiON and PEDOT-TiON surfaces.

reached 52° much >9° for the TiON anode, also implying the higher hydrophobicity of the PEDOT-TiON anode. Consequently, this further validates that the unique hydrophobic mechanism is attributed to the synergy structure of PEDOT-TiON. The calculated stable adsorption energy for one potassium ion on the interface between PEDOT-TiON composite and TiON nanowires is ≈−0.812 and −0.769 eV, respectively. The results suggest that the PEDOT-TiON composite exhibits enhanced adsorption behavior toward potassium ions compared to pristine TiON nanowires, indicating that the presence of a PEDOT coating layer does not impede K^+ insertion into the TiON substrate but rather provides more abundant electrochemical reaction sites.

The MBSH device was assembled by PEDOT-TiON nanowires microelectrodes as anode and Ni $(OH)_2$ nanostructure microelectrodes as cathode, and covered with the 1 M KOH-CMC gel electrolyte. As shown in Figure S16, both CV curves of the PEDOT-TiON nanowires and $Ni(OH)_2$ nanostructure microelectrodes exhibit stable electrochemical reactions within working voltage windows of −1.3 to 0 V and 0 to 0.6 V, respectively. However, such a deep reaction depth leads to increased polarization and structural collapse, thereby resulting in suboptimal cycle performance. The CV performance of MBSH devices was characterized within a voltage range of 0 to 2 V, while the GCD performance was evaluated within a voltage range of 0 to 1.9 V. **Figure** 5a illustrates an increase in CV scan rate from 10 to 50 mV s^{-1} resulting in a consistently expanding area under the CV curve, showing the high reversible reaction. The GCD curves exhibit a distinct stepped-sloping platform with remarkable symmetry within the voltage range of 0 to 1.9 V, indicating exceptional reversible capacity. At a current density of 2 mA cm^{-2}, the device demonstrates notable areal-specific capacity (49.3 μAh cm^{-2}). As depicted in Figure 4c, when the current density increases to 100 mA cm^{-2}, the areal specific capacity decreases to 22.8 μAh cm^{-2} while maintaining an impressive capacity retention rate of 46.2%, demonstrating outstanding power characteristics for the PEDOT-TiON//$Ni(OH)_2$ MBSH device. Figure 5d shows the Ragone plot of our PEDOT-TiON//Ni $(OH)_2$ MBSH device, the previously reported N-SWCNTs MSCs, and other micro energy storage devices. The PEDOT-TiON//Ni $(OH)_2$ MBSH device has an areal energy density of 55.6 μWh cm^{-2} while maintaining an area power density of 2.3 mW cm^{-2}. When the area power density is increased to up to 77.5 mW cm^{-2}, the device can thus maintain an area energy density of 17.7 μWh cm^{-2}. These excellent electrochemical performances have exceeded those of many reported MSCs, such as: Al electrolytic capacitors;[23] N-SWCNTs MSCs,[24] PPy@rGO//PEDOT@rGO AMSC,[25] VZNGC MSCs,[26] O-LIG MSCS,[27] and Zn_xMnO_2//ACC Zn-HSC.[28]

The long-term cyclic performance of MESD is widely acknowledged as a practical indicator of their suitability as power

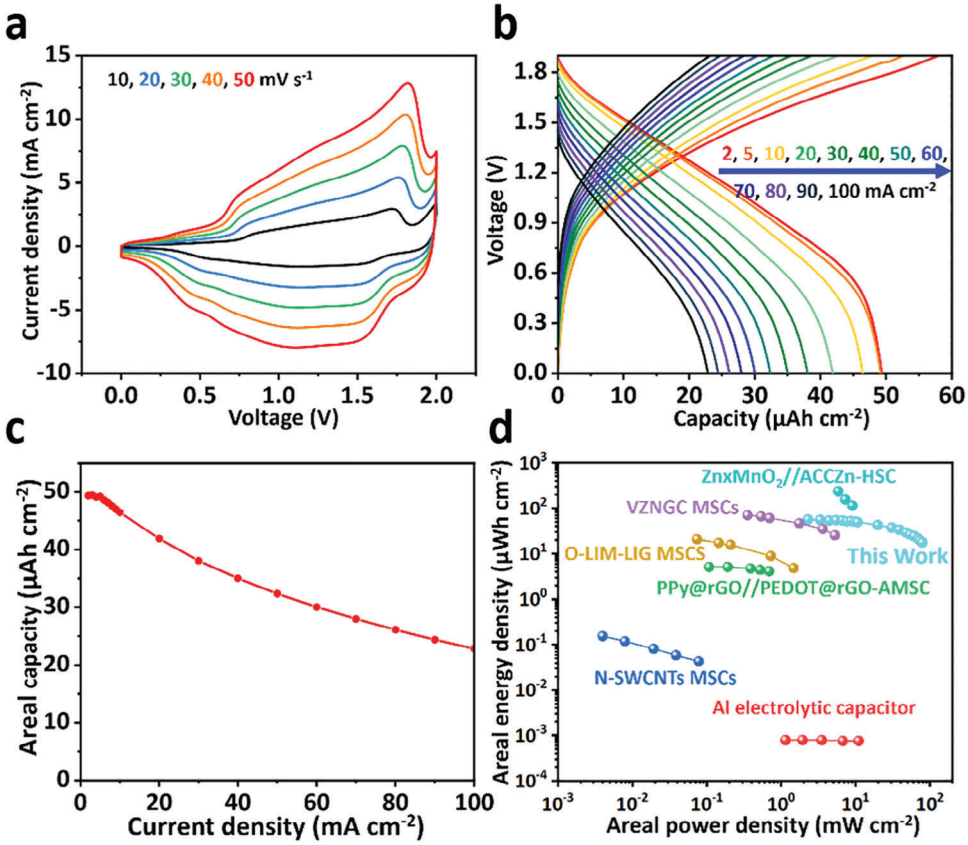

Figure 5. a,b) CV and GCD curves of the PEDOT-TiON//$Ni(OH)_2$ MBSH in 1 M KOH-CMC gel electrolyte. c) Areal capacity of MBSH device at different current densities. d) Ragone plots showing the areal energy/power densities of MBSH in comparison with other reported MSCs.

sources, particularly for on-chip integration into chip circuits. However, due to the need for replacement after a decline in cyclic performance, there is a significant increase in overall cost and an integration challenge arises. Therefore, ensuring high cycling performance is crucial for on-chip MESD. Surprisingly, the PEDOT-TiON//$Ni(OH)_2$ MBSH device exhibits an exceptionally long cycling lifespan of up to 30 000 cycles and demonstrates excellent capacitance retention of 71.8%, thereby presenting significant advantages over other MESD devices[29,30] (see Figure S17 and Table S1, Supporting Information) and showcasing its immense potential for high-reliability applications. The observed increase followed by a subsequent decrease in capacitance can be attributed to the continuous oxidation of $Ni(OH)_2$ nanostructure microelectrodes. The field of skin electronic/portable sensors is developing rapidly, relying on thin-film devices to collect large amounts of human data. However, the current commercial energy storage devices in this field are limited to small button batteries, leading to an overall increase in thickness. The current commercial patch-type blood glucose meter, for instance, exhibits a thickness of ≈5 mm. This requires reliance on a strong binder fixed at the arm, reducing the comfort while wearing it. From this perspective, we can utilize the PEDOT-TiON//$Ni(OH)_2$ MBSH device in various fields as an energy resource supply (**Figure 6a**). The series MBSH device can power an electronic timer and a red LED (Figure 6b,c). Additionally, a single MBSH device exhibits the capability to provide power to a commercially available resistive thin-film pressure sensor (Figure 6d). As depicted in Figure 6e, its planar configuration aligns with that of the planar sensor and allows for integration in commercial applications. During the pressing process, it exhibits a sharp response current curve and quick responsiveness; the intensity of the response current is correlated with the applied pressure intensity. Moreover, it maintains excellent response capability even during prolonged periods of pressing (Figure 6f). Therefore, our devices possess promising prospects for application in pressure sensors.

3. Conclusion

In summary, an MBSH device with ultrahigh power density and ultralong cycling performance has been achieved. Benefiting from the synergy of superior electronic conductivity electrode material and high ions conducting polymer, the obtained PEDOT-TiON microelectrode not only shows better electrochemical performance than the pristine TiON microelectrode, but also effectively restrains side reaction due to the unique hydrophobic mechanism. Furthermore, this MBSH device has demonstrated a significantly prolonged lifespan compared to previously reported microenergy storage devices, exhibiting an impressive capacity retention rate of 71.8% after undergoing 30 000 cycles at 10 mA cm^{-2}. At the same time, DFT, ex situ Raman and multidimensional characterizations reveal the working mechanism of the PEDOT-TiON nanowires microelectrode. Therefore, this

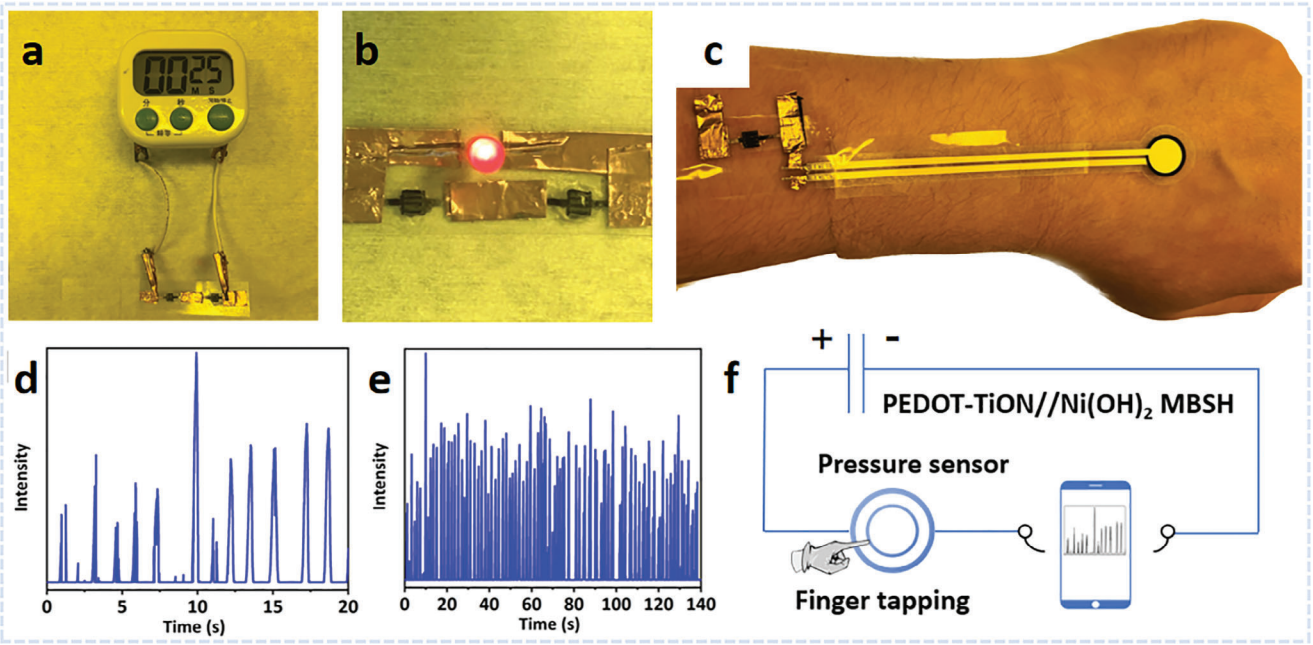

Figure 6. Digital photo images of the various applications powered by PEDOT-TiON//$Ni(OH)_2$ MBSH devices a) an electronic timer, b) a red LED, and c) a pressure sensor. Pressure response signal with d) short and e) long time. f) Work diagram.

work will indeed enlighten the new insight for the development of high electrochemical performance, long serve lifespan, and excellent integration for the next generation micro energy storage device.

4. Experiment Section

Chemical. Titanium dioxide (TiO_2, anatase), Sodium dodecyl sulfate (SDS), Nickel sulfate hexahydrate ($NiSO_4{\cdot}6H_2O$), Ammonium sulfate ($(NH_4)_2SO_4$), Nickel chloride hexahydrate ($NiCl_2{\cdot}6H_2O$), Potassium hydroxide (KOH), Sodium hydroxide (NaOH), Magnesium nitrate hexahydrate ($Mg(NO_3)_2{\cdot}6H_2O$), 3,4-ethylenedioxythiophene (EDOT), Carboxyl Methyl Cellulose (CMC). All the chemicals were used without further purification.

Density Functional Theory Simulation (DFT): The spin-polarized DFT calculations were performed within the Vienna Ab-initio Simulation Package (VASP). Generalized gradient approximation (GGA) with the Perdew-Burke-Ernzerhof (PBE) parameterization was selected to give accurate exchange-correlation energy of electrons. The weak and long-range interactions were described by the DFT-D3 method with BJ-damping. The plane-wave basis set with a kinetic energy cutoff of 520 eV was selected for all self-consistent field calculations, and the k-point was set to 3 × 3 ×1. The slabs were relaxed until the total energy differences were $<1.0 \times 10^{-5}$ eV per atom and the atomic force <-0.02 eV $Å^{-1}$.

Synthesis of $H_2Ti_3O_7$ Nanowires: $H_2Ti_3O_7$ NWs were synthesized by a reported hydrothermal method.[31] Briefly, TiO_2 (anatase, 2 g) was added into NaOH solution (30 mL, 15 M) under magnetic stirring for 1 h. Then, the suspension was transferred to a 50 mL Teflon-lined stainless-steel autoclave and heated in an oven at 180 °C for 72 h. After cooling down to room temperature, the product was stirred in HCl (0.1 M) solution for 24 h. Finally, the material obtained after filtration was rinsed several times with deionized (DI) water and alcohol, followed by drying at 70 °C for 12 h.

Synthesis of $H_2Ti_3O_7$ Microelectrode: Briefly, $H_2Ti_3O_7$ NWs (20 mg) were dispersed in alcohol (20 mL) with $Mg(NO_3)_2{\cdot}6H_2O$ (5 mg) as a surfactant. After ultrasonic treatment for 1 h, the color of the EP suspension became white. An industrially processed Ti interdigital microelectrode and a Pt foil electrode were employed as negative and positive electrodes, respectively. Electrophoresis was conducted on the Ti interdigital microelectrode at a constant voltage of 30 V for 5 min. Afterward, all the fingers of Ti interdigital microelectrode turned white, and a fluffy layer of $H_2Ti_3O_7$ NWs containing ethanol was physically absorbed into the microelectrode. After drying at 100 °C with an electrode holder on the heating stage, a dense $H_2Ti_3O_7$ NWs microelectrode was obtained.

Fabrication of PEDOT-TiON NW Microelectrode: PEDOT-TiON NW microelectrodes were fabricated using two main processes. On the one hand, the $H_2Ti_3O_7$ NW microelectrode was transferred to a combustion boat. By annealing at 800 °C for 3 h in NH_3 flow, the TiON NW microelectrode was fabricated. On the other hand, the PEDOT-TiON NW microelectrode was fabricated through a CV EDP with a CHI760D electrochemical workstation under a typical three-electrode electrochemical system. The TiON NW microelectrode was employed as a working electrode directly, a Pt foil electrode was employed as a counter electrode, and a saturated Ag/AgCl electrode was employed as a reference electrode. The typical deposition was performed in a mixed solution of EDOT (100 µL), SDS (50 mg), and DI water (20 mL) with the potential window of 0–1.2 V (vs Ag/AgCl) at 50 mV s^{-1} for 80 cycles. The PEDOT-TiON NW microelectrode was rinsed with DI water and then dried at 70 °C for 30 min.

Synthesis of $Ni(OH)_2$ Nanostructure Microelectrode: First, with the Pt foil electrode as the counter electrode and Ag/AgCl electrode as the reference electrode, the Ni interdigital microelectrode formed the three-electrode system, whereas the electrolyte is a mixed solution of Nickel sulfate (0.1 M) and Ammonium sulfate (0.5 M). Then the electrochemical deposition proceeded in the CHI760E electrochemical workstation for 50 s with a constant voltage of −4.5 V. The nickel interdigital microelectrode was then fully washed with deionized (DI) water. Following, the microelectrode was used in a CV process at 10 mv s^{-1} after 40 cycles with 1 M KOH aqueous solution as the electrolyte. Finally, rinse several times with deionized (DI) water and the $Ni(OH)_2$ nanostructure microelectrode was successfully prepared.

Preparation of the Electrolytes: The gel electrolyte was fabricated as follows, 1 M KOH solution (1.122 g KOH dissolved in 20 mL deionized water) was mixed with the Carboxyl Methyl Cellulose (CMC, 2 g) under magnetic stirring at 85 °C over 2 h to form the viscous solution, and then cooled down naturally in the ambient environment.

Fabrication of the PEDOT-TiON//Ni(OH)$_2$ MBSH Device: The PEDOT-TiON//Ni(OH)$_2$ based MBSH device was assembly by pasting PEDOT-TiON anode and Ni(OH)$_2$ cathode microelectrodes on a PET film by cyanoacrylate glue under optical alignment. After solidification of cyanoacrylate glue, the pre-obtained KOH/CMC gel electrolyte was coated onto the surface of the MBSH device, and the PEDOT-TiON//Ni(OH)$_2$ MBSH device was assembled.

Materials and Devices Characterization: Scanning Electron Microscopy (SEM) images were obtained with a JEOL JSM-7100F SEM at an acceleration voltage of 20.0 kV. Energy dispersive X-ray spectroscopy (EDS) results were recorded by an Oxford IE250 system. X-ray photoelectron spectroscopy (XPS) results were recorded by the VG Multi Lab 2000.

Methods of Calculations: The CV and GCD curves of the PEDOT-TiON and Ni(OH)$_2$ micro-electrode were investigated by a CHI760D. The EIS tests of Porous Ni and PEDOT-TiON NW microelectrodes were conducted by an Autolab 302N. The electrochemical performances of MBSH devices were measured by a two-electrode system. Here the electrochemical performance of micro-electrode material can be calculated from the examined results.

The areal capacity (C_h) of PEDOT-TiON micro-electrode is using the following equation:

$$C_h = \frac{\int I dt}{A \Delta V} \tag{2}$$

where the I, Δt, A, and ΔV are the discharge current, the discharge time after IR drop, the print area of half of the full device (0.07 cm^2), and the potential window, respectively.

The areal capacity (C_h) of Ni(OH)$_2$ micro-electrode is using the following equation:

$$C_h = \frac{\int I dt}{A} \tag{3}$$

where the I, Δt and A are the discharge current, the discharge time after IR drop, the print area of half of the full device (0.07 cm^2), respectively.

The areal capacity (C_f) of PEDOT-TiON//Ni(OH)$_2$ based MBSH device is using the following equation:

$$C_f = \frac{\int I dt}{A} \tag{4}$$

where the I, Δt *and* A are the discharge current, the discharge time after IR drop, and the print area of the full device (0.14 cm^2), respectively.

The areal energy density (E_a) and areal power density (P_a) are calculated using the following equation:

$$E_a = \frac{\int_0^t IV(t)\ dt}{A} \tag{5}$$

$$P_a = \frac{E_a}{t} \times 3600 \tag{6}$$

where t refers to the discharge time, I is the discharge current, $V(t)$ is the discharge voltage at t, dt is the time differential, and A is the print area of the full device.

Supporting Information

Supporting Information is available from the Wiley Online Library or from the author.

Acknowledgements

This work was supported by the National Natural Science Foundation of China (52172233, 52272234), the National Key Research and Development Program of China (2020YFA0715000), the Independent Innovation Project of Hubei Longzhong Laboratory (2022ZZ-20), the Key Research and Development Program of Hubei (2022BAA027) and the Postdoctoral Fellowship Program of CPSF (GZB20240581).

Conflict of Interest

The authors declare no conflict of interest.

Data Availability Statement

The data that support the findings of this study are available from the corresponding author upon reasonable request.

Keywords

bi-functional composite microstructure, high cycling performance, high power density, micro battery-supercapacitor hybrid device

Received: July 25, 2024
Revised: September 22, 2024
Published online: October 10, 2024

[1] a) A. Tyagi, K. M. Tripathi, R. K. Gupta, *J. Mater. Chem. A* **2015**, *3*, 22507; b) X. Wang, Y. Chen, O. G. Schmidt, C. Yan, *Chem. Soc. Rev.* **2016**, *45*, 1308; c) Z.-S. Wu, X. Feng, H.-M. Cheng, *Natl. Sci. Rev.* **2014**, *1*, 277; d) C. Gao, Y. Gu, Y. Zhao, L. Qu, *Energy Material Advances* **2022**, *2022*, 9804891; e) F. Lv, Z. Hong, Z. Ahmad, H. Li, Y. Wu, Y. Huang, *Energy Material Advances* **2023**, *4*, 0043.

[2] a) H. Wang, R. Guo, H. Li, J. Wang, C. Du, X. Wang, Z. Zheng, *Chem. Eng. J.* **2022**, *429*, 132196; b) N. A. Kyerematen, R. Hahn, *ACS Energy Lett.* **2018**, *3*, 1172.

[3] a) J. Ni, A. Dai, Y. Yuan, L. Li, J. Lu, *Matter* **2020**, *2*, 1366; b) X. Wang, Z. S. Wu, *EcoMat* **2020**, *2*, e12042; c) S. Wu, Z. Hu, P. He, L. Ren, J. Huang, J. Luo, *eScience* **2023**, 3.

[4] a) H. Zhang, Y. Cao, M. O. L. Chee, P. Dong, M. Ye, J. Shen, *Nanoscale* **2019**, *11*, 5807; b) M. Beidaghi, Y. Gogotsi, *Energy Environ. Sci.* **2014**, *7*, 867; c) H. Hu, Z. Pei, C. Ye, *Energy Storage Mater.* **2015**, *1*, 82.

[5] a) W. Zuo, R. Li, C. Zhou, Y. Li, J. Xia, J. Liu, *Adv. Sci.* **2017**, *4*, 1600539; b) F. Xing, Z. Bi, F. Su, F. Liu, Z. S. Wu, *Adv. Energy Mater.* **2022**, *12*, 2200594.

[6] M. He, K. Fic, E. Frąckowiak, P. Novák, E. J. Berg, *Energy Environ. Sci.* **2016**, *9*, 623.

[7] a) Y. Li, J. Zhou, T. Zhang, T. Wang, X. Li, Y. Jia, J. Cheng, Q. Guan, E. Liu, H. Peng, B. Wang, *Adv. Funct. Mater.* **2019**, *29*, 1808117; b) F. Zheng, Y. Yang, Q. Chen, *Nat. Commun.* **2014**, *5*, 5261.

[8] a) S. Mahadik, S. Surendran, J. Y. Kim, G. Janani, D.-K. Lee, T.-H. Kim, J. K. Kim, U. Sim, *J. Mater. Chem. A* **2022**, *10*, 14655; b) Q. Wei, T. Huang, X. Huang, B. Wang, Y. Jiang, D. Tang, D. L. Peng, B. Dunn, L. Mai, *Interdisciplinary Materials* **2023**, *2*, 434.

[9] a) P. Qin, C. Huang, B. Gao, C. Pi, J. Fu, X. Zhang, K. Huo, P. K. Chu, *Appl. Surf. Sci.* **2020**, *503*, 144293; b) L. Lu, Y. Xie, *New J. Chem.* **2017**, *41*, 335.

[10] a) X. Lu, G. Wang, T. Zhai, M. Yu, S. Xie, Y. Ling, C. Liang, Y. Tong, Y. Li, *Nano Lett.* **2012**, *12*, 5376; b) X. Zhou, C. Shang, L. Gu, S. Dong, X. Chen, P. Han, L. Li, J. Yao, Z. Liu, H. Xu, Y. Zhu, G. Cui, *ACS Appl. Mater. Interfaces* **2011**, *3*, 3058.

[11] H. Qi, S. Yick, O. Francis, A. Murdock, T. van der Laan, K. Ostrikov, Z. Bo, Z. Han, A. Bendavid, *Energy Storage Mater.* **2020**, *26*, 138.

[12] Y. Xie, X. Fang, *Electrochim. Acta* **2014**, *120*, 273.

[13] a) B. Lu, H. Yuk, S. Lin, N. Jian, K. Qu, J. Xu, X. Zhao, *Nat. Commun.* **2019**, *10*, 1043; b) T. Horii, H. Hikawa, M. Katsunuma, H. J. P. Okuzaki, *Polymer* **2018**, *140*, 33; c) Y. Jiang, X. Dong, L. Sun, T. Liu, F. Qin, C. Xie, P. Jiang, L. Hu, X. Lu, X. Zhou, W. Meng, N. Li, C. J. Brabec, Y. Zhou, *Nat. Energy* **2022**, *7*, 352; d) P. Liu, M. Huang, X. Chen, Y. Gao, Y. Li, C. Dong, G. Wang, *Interdisciplinary Materials* **2023**, *2*, 423.

[14] W. Yang, Y. Zhu, Z. Jia, L. He, L. Xu, J. Meng, M. Tahir, Z. Zhou, X. Wang, L. Mai, *Adv. Energy Mater.* **2020**, *10*, 2001873.

[15] Z. Li, Q. He, X. Xu, Y. Zhao, X. Liu, C. Zhou, D. Ai, L. Xia, L. Mai, *Adv. Mater.* **2018**, *30*, 1804089.

[16] a) Z. Hao, L. Xu, Q. Liu, W. Yang, X. Liao, J. Meng, X. Hong, L. He, L. Mai, *Adv. Funct. Mater.* **2019**, *29*, 1808470; b) Y. Li, R. Zhang, J. Qian, Y. Gong, H. Li, C. Wu, Y. Bai, F. Wu, *Energy Material Advances* **2023**, 4.

[17] a) C. Xu, J. Liao, C. Yang, R. Wang, D. Wu, P. Zou, Z. Lin, B. Li, F. Kang, C.-P. Wong, *Nano Energy* **2016**, *30*, 900; b) M. Li, Y. Li, Q. Cu, Y. Li, H. Li, Z. Li, M. Li, H. Liao, G. Li, G. Li, X. Wang, *Energy Material Advances* **2023**, 4.

[18] a) Y. Jiang, J. Liu, *Energy & Environmental Materials* **2019**, *2*, 30; b) J. Yue, S. Li, S. Chen, J. Yang, X. Lu, Y. Li, R. Zhao, C. Wu, Y. Bai, *Energy Material Advances* **2023**, 4.

[19] L. Miao, J. Wu, J. Jiang, P. Liang, *J. Phys. Chem. C* **2012**, *117*, 23.

[20] a) M. P. Ravikumar, T.-A. Quach, B. Urupalli, M. K. Murikinati, S. Muthukonda Venkatakrishnan, T.-O. Do, S. Mohan, *Environ. Res.* **2023**, *229*, 115961; b) P. Urbankowski, B. Anasori, T. Makaryan, D. Er, S. Kota, P. L. Walsh, M. Zhao, V. B. Shenoy, M. W. Barsoum, Y. Gogotsi, *Nanoscale* **2016**, *8*, 11385.

[21] R. Kumar, B. K. Singh, A. Soam, S. Parida, V. Sahajwalla, P. Bhargava, *Nanoscale Advances* **2020**, *2*, 2376.

[22] a) X. J. Wang, K. Y. Wong, *Thin Solid Films* **2006**, *515*, 1573; b) L. Wang, T. Shu, S. Guo, Y. Lu, M. Li, J. Nzabahimana, X. Hu, *Energy Storage Mater.* **2020**, *27*, 150; c) T. N. M. Cervantes, D. C. Bento, E. C. R. Maia, D. A. M. Zaia, E. Laureto, M. A. T. da Silva, G. J. Moore, H. de Santana, *J. Mater. Sci.: Mater. Electron.* **2012**, *23*, 1916.

[23] M. F. El-Kady, R. B. Kaner, *Nat. Commun.* **2013**, *4*, 1475.

[24] H. Dong, L. Zhang, Y. Liao, K. Huang, C. Lian, X. Zhou, Z. Zhang, E. I. Kauppinen, Z. S. Wu, *Adv. Funct. Mater.* **2023**, *33*, 2301103.

[25] M. Tahir, L. He, W. Yang, X. Hong, W. A. Haider, H. Tang, Z. Zhu, K. A. Owusu, L. Mai, *J. Energy Chem.* **2020**, *49*, 224.

[26] H. Zhou, G. Zhu, S. Dong, P. Liu, Y. Lu, Z. Zhou, S. Cao, Y. Zhang, H. Pang, *Adv. Mater.* **2023**, *35*, 2211523.

[27] S. Deshmukh, K. Ghosh, M. Pykal, M. Otyepka, M. Pumera, *ACS Nano* **2023**, *17*, 20537.

[28] Q. Chen, J. Jin, Z. Kou, C. Liao, Z. Liu, L. Zhou, J. Wang, L. Mai, *Small* **2020**, *16*, 2000091.

[29] a) Y. Liu, S. Zheng, J. Ma, Y. Zhu, J. Wang, X. Feng, Z.-S. Wu, *J. Energy Chem.* **2021**, *63*, 514; b) W. Fan, Q. Wang, K. Rong, Y. Shi, W. Peng, H. Li, Z. Guo, B. B. Xu, H. Hou, H. Algadi, S. Ge, *Nano-Micro Lett.* **2023**, *16*, 36. c) Y.-R. Wang, F. Zhang, J.-M. Gu, X.-Y. Zhao, R. Zhao, X. Wang, T.-H. Wu, J. Wang, J.-D. Wang, D.-S. Wang, *Rare Met.* **2023**, *43*, 138; d) X. Wang, Y. Li, S. Wang, F. Zhou, P. Das, C. Sun, S. Zheng, Z. S. Wu, *Adv. Energy Mater.* **2020**, *10*, 2000081; e) K. Niu, J. Shi, L. Zhang, Y. Yue, S. Mo, S. Li, W. Li, L. Wen, Y. Hou, L. Sun, S. Yan, F. Long, Y. Gao, *Adv. Sci.* **2023**, *11*, 2305524;

[30] a) Y. Lu, Z. Wang, M. Li, Z. Li, X. Hu, Q. Xu, Y. Wang, H. Liu, Y. Wang, *Adv. Funct. Mater.* **2023**, *34*, 2310966; b) W. Yang, L. Xu, W. Luo, M. Huang, K. Fu, R. Song, C. Han, R. Tu, J. Shi, L. Mai, *Matter* **2023**, *6*, 3006; c) X. Li, X. Jin, Y. Wang, X. Zhang, D. Li, J. Wang, M. Yuan, J. Liu, Y. Zhao, *Adv. Funct. Mater.* **2023**, *34*, 2314060; d) X. Jin, L. Song, C. Dai, Y. Xiao, Y. Han, X. Li, Y. Wang, J. Zhang, Y. Zhao, Z. Zhang, N. Chen, L. Jiang, L. Qu, *Adv. Mater.* **2022**, *34*, 2109450.

[31] J. Dong, Y. Jiang, Q. Li, Q. Wei, W. Yang, S. Tan, X. Xu, Q. An, L. Mai, *J. Mater. Chem. A* **2017**, *5*, 10827.